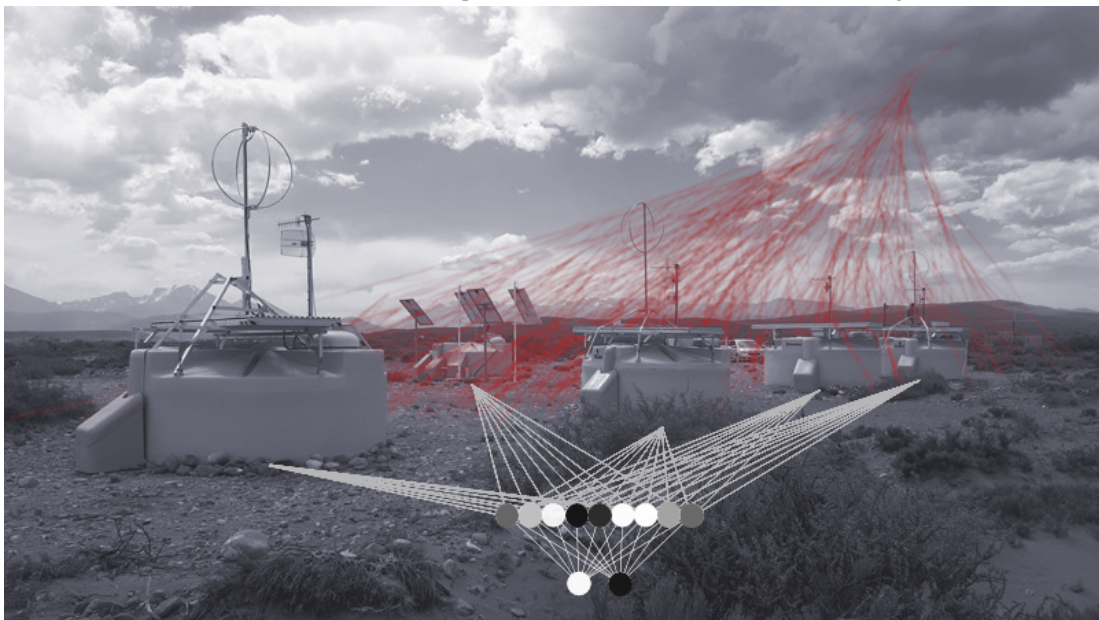


Harry Potter and the Neural network triggers for the surface detector of the Pierre Auger Observatory



Master's thesis by

Paul Filip

at the Institute for Astro Particle Physics

First Reviewer: Prof. Dr. Ralph Engel

Second Reviewer: Prof. Dr. Guido Drexlin

Processing time: 01.04.2022 – 31.03.2022

Review and Declaration

This thesis has been accepted by the first reviewer of the master thesis.

Karlsruhe, TBD

Prof. Dr. Ralph Engel

I declare that the work in this thesis was carried out in accordance with the requirements of the university's regulations and that it has not been submitted for any other academic award. Except where indicated by specific reference in the text, the work is the candidate's own work. Work done in collaboration with, or with the assistance of, others is indicated as such.

Karlsruhe, TBD

Paul Filip

Contents

1	Physics of cosmic rays	1
1.1	History	1
1.2	Acceleration	1
1.2.1	Diffusive shock acceleration (Fermi I)	2
1.2.2	Stochastic scattering acceleration (Fermi II)	3
1.2.3	Centrifugal acceleration in rotating \vec{B} -fields	3
1.2.4	Direct electrostatic acceleration	4
1.2.5	Other types & general classification	4
1.2.6	Acceleration of uncharged particles	5
1.3	Propagation	6
1.3.1	Intergalactic propagation & transport equation	6
1.3.2	Extragalactic propagation & GZK-Cutoff	8
1.4	Composition	9
1.5	Energy spectrum	10
1.5.1	The proton knee $E \approx 10^{15}$ eV	10
1.5.2	The iron knee $E \approx 10^{17}$ eV	11
1.5.3	The Ankle $E \approx 10^{18}$ eV	12
1.5.4	The suppression $E \approx 10^{20}$ eV	12
2	Extensive air showers	13
2.1	Electromagnetic showers	13
2.2	Hadronic showers	14
2.3	Superposition principle	16
3	The Pierre Auger Observatory	17
3.1	Fluorescence Detector (FD)	17
3.2	Surface Detector (SD)	19
3.2.1	Data acquisition (DAQ)	19
3.2.2	Offline calibration	20
3.2.3	Online calibration	24
3.3	Event Reconstruction	24
3.3.1	Trigger procedure	25
3.3.2	Core position	26
3.3.3	Arrival direction	26
3.3.4	Energy estimation	27
3.3.5	Primary particle	27

1 Physics of cosmic rays

This chapter aims to introduce the general physical principles underlying the analysis presented in this work. For this purpose, an overview of the origin, composition and energy spectrum of cosmic rays is given in section 1.1, section 1.2, and section 1.5 respectively.

1.1 History

A first hint at the existence of high-energy particles in the upper atmosphere was given by Hess in 1912, who found that the discharge rate of an electroscope is altitude-dependant. Millikan coined the term cosmic "rays" for these particles, as he argued the ionizing radiation must be part of the electromagnetic spectrum [1]. This was later, at least partially, falsified with the discovery of the east-west effect [2]. Hess' observation however withstood the tests of time and was ultimately recognized with the Nobel prize in physics in 1936 [3]. Two years later, in 1938, Pierre Auger showed via coincidence measurements that cosmic rays in fact originate from outer space, and gave a first description of extensive air showers [4]. Another 60 years later, the Pierre Auger collaboration would adopt his experimental setup and name in their search for cosmic rays of the highest energies.

In the meantime, numerous results from different cosmic ray detectors all over the globe have helped propel the related fields of particle physics, astro physics and cosmology to new insights. Observations from cosmic ray physics serve as a valuable cross-check to the hadronic interaction models developed e.g. at CERN [5]. New theories modeling the final moments in the life of stars have arisen thanks to results from e.g. Kamiokande [6]. Last but not least publications by the Pierre Auger collaboration regarding the CR energy spectrum and flux help refine knowledge of our cosmic neighbourhood [7, 8].

1.2 Acceleration

Cosmic rays whose kinetic energy far exceeds their rest energy must originate from some of the most extreme environments in space. In particular, regions with large (either in field strength or spatial extent) electromagnetic fields, where charged particles can be accelerated to significant fractions of to the speed of light, via the Lorentz force.

The question how particles are accelerated to the extremely high energies observed on earth is an active area of research. Since the discovery of cosmic rays, several candidate mechanisms and interactions have been identified and will be discussed now.

1.2.1 Diffusive shock acceleration (Fermi I)

Super Nova Remnants (SNR) typically feature a plasma sphere propagating outwards from the former stars core into the Inter Stellar Medium (ISM), in this region of plasma any magnetic field lines will be comoving, according to Alfvén's theorem [9]. First realised by Fermi, such SNR shock fronts serve as source of high-energy CRs [10].

If a low-energy particle is injected into the SNR shock front, it will eventually be reflected by the local \vec{B} -field. If the diffusion length within the plasma is much smaller than the spatial extent of the SNR, the shock front can be modelled as a plane, and the process is analogous to an elastic reflection against a wall. Consequently, if $\frac{d\vec{B}}{dt} = 0$, this does not cause the particle to gain any energy, espically because $W = \vec{F}_L \cdot \vec{r} \propto (\vec{v} \times \vec{B}) \cdot \vec{r} = 0$. However, because the \vec{B} -field is moving radially outward alongside the plasma, a net energy gain of

$$\Delta E = +\beta_{\text{SNR}} \cdot E_0 \quad (1.1)$$

arises, where $\beta_{\text{SNR}} = |\vec{v}_{\text{SNR}}| / c$ and E_0 are the velocity of the shock-front and the initial energy of the particle. From chapter 7 in [10] it follows that ionization losses within the shock front are not completely negligible. Hence a particle must have a sufficient energy such that ΔE in Equation 1.1 exceeds possible ionization losses. The corresponding threshold for the primary energy above which acceleration occurs is dubbed the injection energy, and is of the order of 200 MeV for protons.

Furthermore, because typically $\beta_{\text{SNR}} \leq 0.10$ a single acceleration cycle is not enough to explain the CR energies observed on earth. Instead, multiple cycles are needed. This requires additional, focusing \vec{B} -fields, provided for example by the ISM, which alter the trajectory of injected particles such that they can be reflected off the shock-front again.

With each cycle, the particles rigidity $R = |\vec{p}|c / q$ increases, until its gyroradius $\rho = R/|\vec{B}|$ exceeds the spatial extent of the focusing \vec{B} -field and the particle escapes into space. With an effective ejection probability p per cycle, the energy after n cycles and the expected flux w.r.t energy, $\Phi(E)$, becomes roughly

$$E(n) = E_0 (1 + \beta_{\text{SNR}})^n. \quad (1.2)$$

$$\begin{aligned}
N(n) &= N_0 (1 - p)^n \\
\Leftrightarrow \log \left(\frac{N(n)}{N_0} \right) &= n \cdot \log(1 - p) \\
\Leftrightarrow &\stackrel{(1.2)}{=} \log \left(\frac{E(n)}{E_0} \right) \frac{\log(1 - p)}{\log(1 + \beta_{\text{SNR}})} \\
\Leftrightarrow N(E) &= N_0 \cdot \left(\frac{E(n)}{E_0} \right)^{\log(1-p) / \log(1+\beta_{\text{SNR}})} \\
\Rightarrow \Phi(E) &= \frac{dN}{dE} \propto E(n)^{\alpha-1}, \tag{1.3}
\end{aligned}$$

where $\alpha = \frac{\log(1-p)}{\log(1+\beta_{\text{SNR}})}$ in Equation 1.3 is a spectral coefficient whose exact value will depend on the age of the SNR (β_{SNR} decreases with age), the injected particle (different primaries have different injection energies and ejection probabilities), as well as many other factors that are often not known a priori. It can be observed that the expected spectrum is a power law in the ranges from injection energy to a cutoff at the highest energies, which arises due to the finite lifetime of SNRs.

Results from several studies (e.g. [8, 11, 12]) hint that the presented first order Fermi acceleration mechanism is the main source of galactic CRs, extrasolar particles that originate from within the milky way, with energies ranging up to orders $O(\text{TeV})$.

1.2.2 Stochastic scattering acceleration (Fermi II)

Second order (or Stochastic) Fermi acceleration is the more general case of subsection 1.2.1 and represents the original idea developed by Fermi in [10]. The underlying principle of scattering particles off plasma clouds remains unchanged. However, if the diffusion length within the cloud exceeds its radius of curvature, the energy gain per collision instead becomes

$$\Delta E \propto + (\beta_{\text{SNR}})^2 \cdot E_0. \tag{1.4}$$

Logically, this represents a much more inefficient acceleration mechanism, but is nevertheless observed in nature under certain circumstances (c.f. [13]).

1.2.3 Centrifugal acceleration in rotating \vec{B} -fields

Some astrophysical objects such as pulsars or Active Galactic Nuclei (AGNs) possess strong magnetic fields ranging from 1 T for some AGNs [14] to $\approx 10 \text{ GT}$ for magnetars, a subset of pulsars with extremely high magnetic flux densities [15].

If such objects rotate at an angular velocity Ω , which is in general nonzero, charged particles at a radial distance r from the rotation axis will undergo centrifugal acceleration. In particular, their Lorentz factor γ behaves like Equation 1.5 [16].

$$\gamma := \frac{E}{m_0 c^2} = \frac{\gamma_0}{1 - \left(\frac{\Omega r}{c}\right)^2}, \quad (1.5)$$

where m_0 is the rest mass of the particle and γ_0 the prior Lorentz factor before acceleration. It follows that a test particle can in theory gain an arbitrarily high energy from this process by outspiraling towards the light cylinder surface, where $\Omega \cdot r = c$. In reality however, these processes are stopped by e.g. inverse Compton scattering at some point [17]. In any case, [16] and [17] conclude that values of $\gamma \approx 10^7 - 10^8$ are possible, corresponding to protons at $\approx 10 \text{ PeV} - 10 \text{ PeV}$ or iron nuclei at $\approx 500 \text{ PeV} - 5 \text{ EeV}$ energy.

1.2.4 Direct electrostatic acceleration

The presence of non-static \vec{B} -fields implies the existence of (in vacuum) comparably strong \vec{E} -fields and a corresponding electrical potential difference Φ across different regions within the magnetosphere. A back-of-the-envelope calculation reveals that they are (neglecting constant factors) proportional to

$$|\vec{E}| \propto \frac{\Omega r_0}{c} \cdot |\vec{B}|, \quad (1.6)$$

$$\Phi \propto r_0 \cdot |\vec{E}|, \quad (1.7)$$

where r_0 is the radius of the central object rotating at an angular frequency Ω . Consequently, an ion with atomic number Z can be accelerated to energies $E = Z \cdot e \cdot \Phi$, which can in some cases easily exceed 10^{20} eV [18].

Some caveats to this consideration need to be mentioned. Screening effects from plasma clouds surrounding the central body are expected to limit the electrical field strength, and maximum acceleration energy by extension. Additionally, losses via e.g. Bremsstrahlung have been neglected in the above calculation, limiting the maximum attainable energy in theory even further.

1.2.5 Other types & general classification

Several acceleration mechanisms have been discussed. A plethora of other interactions that are able to accelerate elementary particles to fantastic energies remain unmentioned, or even undiscovered, as CR physics is an active area of research. In general though the driving force behind all considered (and non-considered) acceleration mechanisms are thought to be (electro-) magnetic fields. Consequently, the maximum energy a specific

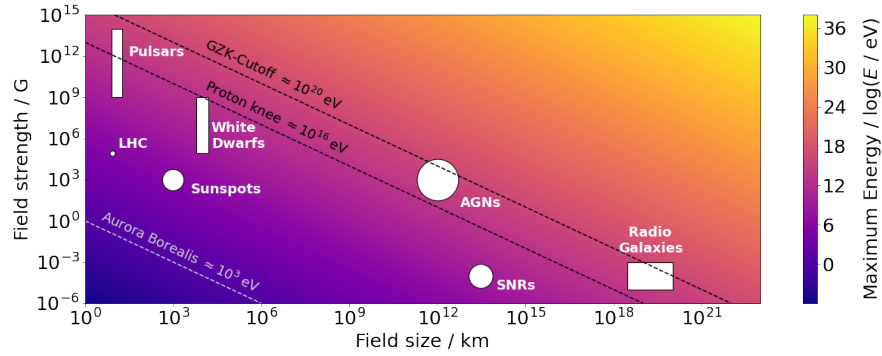


Figure 1.1: Rough estimate of field strength and size of different CR sources as well as the corresponding maximum energy estimated with Equation 1.8 ($\beta = Z = 1$). Isoenergetic lines mark notable points in the energy spectrum discussed in section 1.5.

CR accelerator with magnetic field \vec{B} and size L moving at velocity βc can in theory provide for a particle with charge Ze is given by the Hillas formula [19]:

$$E_{\max} [\text{PeV}] = |\vec{B}| [\mu\text{G}] \cdot L [\text{pc}] \cdot Z \cdot \beta \quad (1.8)$$

This allows for an elegant classification of different cosmic ray sources, in part discussed on the previous pages, according to the Hillas plot shown in Figure 1.1.

1.2.6 Acceleration of uncharged particles

Particles like neutrons, neutrinos or photons possess no electromagnetic charge $q = 0$. Assuming Equation 1.8 holds in these cases, they should thus not appear in the CR spectrum. This is in disagreement with reality, where energies from 100 GeV up to ≈ 100 EeV have been observed [20, 21]. Consequently, additional interaction channels are required to explain the existence of such uncharged CRs.

High energy γ -rays in particular can be created by accelerated, charged particles via Bremsstrahlung. This occurs for example during centrifugal acceleration near pulsars or AGNs (compare subsection 1.2.3). Furthermore, inverse Compton scattering with a high-energy cosmic ray can imply a significant energy gain for a photon [22].

Uncharged CRs are also frequently produced in nuclear interactions, such as e.g. deeply inelastic scattering of charged CRs with the ISM. This espically contributes to the CR photon spectrum, as high energy π^0 are often byproducts of such scattering processes. The uncharged pions then decay into two photons. Furthermore, neutrons or neutrinos can originate from interactions involving the weak force. When a proton converts to $p \rightarrow n + e^+ + \bar{\nu}_e$ during the decay of a UHECR ion, the resulting decay products positron, neutron and electron-antineutrino inherit the parents' energy, and are thus high energy cosmic rays as well.

1.3 Propagation

Once a cosmic ray has been observed coming from some arrival direction (ϕ, θ) , backtracking its trajectory to an eventual origin is, ignoring external factors, in the literal sense, straight forward. It has been shown however that several effects need to be considered for an accurate treatment of CR propagation.

For uncharged CRs (γ, n) , this task is simple. Such particles are not deflected by cosmic \vec{E} and \vec{B} -fields. Possible interactions either demand the destruction of the particle (pair production, weak decay), or occur close to the source (e.g. Compton scattering), in which case the observed arrival direction will still be coincident with the actual source [23]. Gravitational lensing effects in some cases alter the trajectory of extragalactic photons. Such phenomena (if present in the first place) are however well understood in the scope of general relativity, and can be corrected for [24, 25].

1.3.1 Intergalactic propagation & transport equation

Contrary, charged particles (e^\pm, p, ions) propagate along non-trivial paths within galaxies due to deflections from solar- and galactic EM-fields. While the galactic field is coherent over large scales, numerous irregular magnetic domains, seeded in part by individual stars complicate CR propagation to essentially a three-dimensional random walk [26]. It is thus challenging to pinpoint the origin of a charged cosmic ray.

Nevertheless, related queries, such as for example the question whether or not a particle of given energy is likely to be of extragalactic origin can be answered by examining the distribution of cosmic rays within a region of spacetime. The behaviour of a population of n_i particles of type i can be approximately recreated via the below transport equation:

$$\frac{\partial n_i}{\partial t} = \underbrace{Q_i}_{\text{Source}} + \underbrace{\nabla D_i (\nabla n_i)}_{\text{Diffusion}} - \underbrace{\frac{\partial k_i(E)}{\partial E}}_{\text{Energy}} - \underbrace{\left(\frac{n_i}{\tau_{\text{spal}, i}} - \sum_{j>i} \frac{n_j p_{ij}}{\tau_{\text{spal}, j}} \right)}_{\text{Spallation}} - \underbrace{\left(\frac{n_i}{\tau_{\text{rad}, i}} - \sum_{j>i} \frac{n_j d_{ij}}{\tau_{\text{rad}, j}} \right)}_{\text{Weak decay}}$$

- **Source Q_i :**

The source term is responsible for the creation of CR particles (of type i). The exact form of Q_i will depend on the considered creation process. For example, the near instantaneous creation of n_γ photons in a **Gamma-Ray Burst (GRB)** at time t_0 and location \vec{r}_0 can be modelled like $Q_\gamma = n_\gamma \delta(\vec{r} - \vec{r}_0) \delta(t - t_0)$.

- **Diffusion $\nabla D_i (\nabla n_i)$:**

The random walk mentioned above is accounted for in the diffusion term, which takes a similar form to the Stokes-Einstein equation. The diffusion coefficient(s) D_i in general take a tensor form due to anisotropic diffusion in different directions. Furthermore, D_i is different for each particle type, as the deflecting EM-fields couple to the respective charges q_i , which need not be equal in principle.

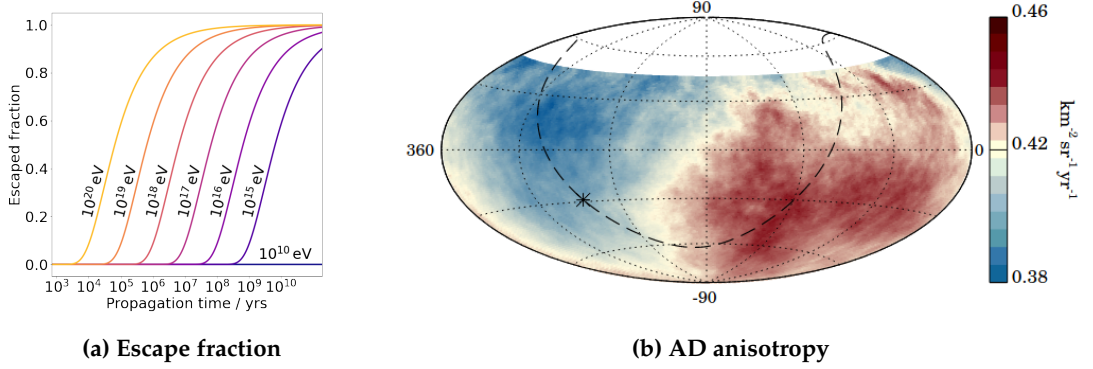


Figure 1.2: (a) $r_{\text{esc.}}(t)$ according to Equation 1.10 for protons of different energies. (b) Dipole in the arrival direction of CRs with $E > 8$ EeV. Image copied from [27].

- **Energy loss** $\partial k_i(E) / \partial E$:

During propagation, a cosmic ray can interact with the ISM, and lose energy in the process. If this happens often enough, the CR is eventually thermalized and does not contribute to the population i any longer. Different interaction channels for different CR types i require different loss models $k_i(E)$ for each type.

- **Spallation** $(n_i / \tau_{\text{spal.}, i} - \sum n_j p_{ij} / \tau_{\text{spal.}, j})$:

Nuclear spallation describes the process of violent disintegration of a target nucleus upon being struck by an energetic projectile. The resulting fragments can retain energies up to the projectiles energy. The spallation term in the transport equation considers both the destruction (first term), as well as creation (second term) of CRs i from heavier types j . It is assumed that spallation from type $j \rightarrow i$ occurs at a constant probability of p_{ij} in a characteristic time frame $\tau_{\text{spal.}, j}$.

- **Weak decay** $(n_i / \tau_{\text{rad.}, i} - \sum n_j d_{ij} / \tau_{\text{rad.}, j})$:

If a particle j is weakly unstable ($\tau_{\text{rad.}, i} < \infty$) there is a nonzero chance d_{ij} it decays into a daughter nuclei of some type i during propagation. The decay term reflects this and describes both decay from heavier and decay into lighter nuclei.

Insights to the physical implications of this parametrization can be gathered from a simplified example. Consider the case of a galaxy with height $2H$ and width W . It is $H \ll W$, and thus only diffusion along the $\pm z$ -direction will be examined. Considering n_0 protons located at $z = 0$ initially, and ignoring interactions with the ISM, the transport equation reduces to the first two terms, with $D = (0, 0, D_z)^T$ and $Q = n_0 \delta(z) \delta(t_0)$.

It can quickly be verified that a solution to the transport equation in this case is given by a normal distribution with mean $\mu = 0$ and standard deviation $\sigma = \sqrt{2D_z t}$. The diffusion coefficient D_z is a measure of how quickly the population spreads out (along the $\pm z$ -direction). According to [28], D_z can be parametrized via the particles energy E_p , and characteristics of the present \vec{B} -fields.

$$D_z = \frac{1}{3} \gamma \cdot \lambda = \frac{1}{3} \frac{E_p}{m_p c^2} \cdot \frac{|\vec{B}| \cdot \langle L_{\vec{B}} \rangle}{\sqrt{\mu_0 \rho_{\text{ISM}}}}, \quad (1.9)$$

where $\langle L_{\vec{B}} \rangle$ is the characteristic length scale of deflecting \vec{B} -fields, μ_0 and ρ_{ISM} are the magnetic vacuum permeability and density of the interstellar medium respectively. After some time t , a fraction $r_{\text{esc.}}(t)$ of particles will have a z -coordinate $|z| > H$, and exit the disc consequently. In reality, this is not equivalent to the particle leaving the galaxy, as large-scale halo structures extend above and below the visible disc [29]. These halos are ignored here. $r_{\text{esc.}}(t)$ can thus be calculated according to Equation 1.10. For some selected energies, a plot of the escaping ratio over time is offered in Figure 1.2a.

$$r_{\text{esc.}}(t) := 1 - \int_{-H}^H \frac{n(z, t)}{n_0} dz \quad (1.10)$$

It can be concluded that low energy CRs do not travel outside their host galaxy within reasonable timeframes. Meanwhile, **Ultra High Energy** CRs (UHECR, $E > 10^{18}$ eV) escape swiftly on ballistic trajectories and can (and often do) have an extragalactic origin, not last also due to the limited energies that CR sources in the milky way can provide (compare section 1.2).

This observation is consistent with a dipole in the **Arrival Direction** (AD) of UHECRs observed by the Pierre Auger observatory. The dipole points roughly in the opposite direction of the galactic core, marked with an asterisk in Figure 1.2b.

1.3.2 Extragalactic propagation & GZK-Cutoff

In the last paragraph the (likely) extragalactic origin of UHECRs was discussed. Such particles must traverse millions of lightyears of extragalactic space before inducing a large air shower on earth. As the energy of these primaries increases above the **Greisen-Zatsepin-Kusmin** threshold (GZK), their propagation through space is thought to be severely impeded. At energies above $\approx 10^{20}$ eV the **Cosmic Microwave Background** (CMB) consisting of photons in the microwave range are blueshifted to energies $E_\gamma > 300$ MeV. A proton with the corresponding energy can thus absorb such CMB photons and convert to its' excited spin state, the Δ^+ -baryon. The Δ^+ -baryon decays nearly instantaneously to (for example) its' ground state again, by radiating away a π^0 [30] and losing energy in the process [30].

The mean free path of this interaction, also labelled GZK horizon is both energy- and primary-dependant (i.e. what kind of cosmic ray is considered). For 75 EeV protons, it is ≈ 100 Mpc. Cosmic rays exceeding the GZK threshold should ergo not be observed from faraway sources, and an overall reduction in flux at these energies should be recorded [31, 32].

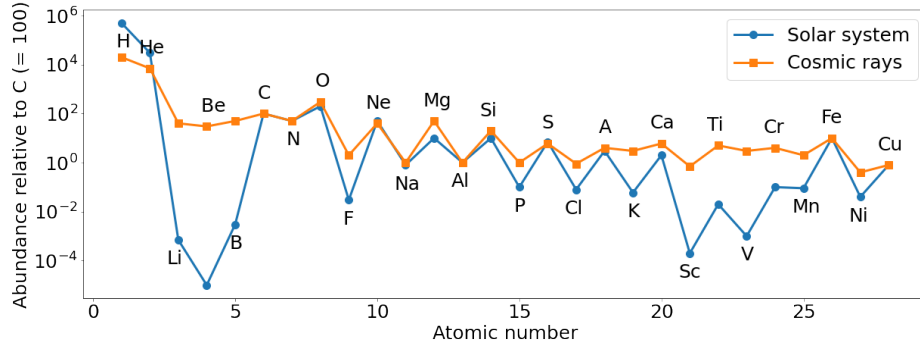


Figure 1.3: Composition expressed as abundance relative to carbon for different sources. The ragged, alternating structure stems from an increased stability of nuclei with an even amount of protons (c.f. for example [37]). Data from [38]

Indeed, results published by the Auger collaboration (see section 1.5) are consistent with this assumption. Whether or not the GZK-suppression is the main cause for this hard spectrum at the highest energies remains unclear for now, but shall hopefully be answered with the ongoing AugerPrime upgrade of Pierre Auger observatory.

1.4 Composition

The composition of CRs largely mirror the relative abundances of elements in the universe with some notable exceptions shown in Figure 1.3. Elements like beryllium (Be) or vanadium (V) are atypical products of supernovae and thus not as common as e.g. oxygen (O) [33, 34] in the solar system. This leads to a dip in the corresponding abundance spectrum. The same dip is not observed in CR primary abundancies. While it is a priori existant upon creation of cosmic rays, but gradually gets "filled up" via e.g. spallation processes during their propagation until an equilibrium state is reached.

This equilibrium state depends sensitively on the characteristic age of cosmic rays, i.e. the mean travel time until a particle escapes the galaxy. Measuring CR composition hence enables the estimation of this parameter. Such an analysis is conducted in [35], where it is found that the observed abundancies are consistent with a characteristic age of 1.7×10^7 yr for such high energy particles.

Contrary, hydrogen (H) and helium (He) are underrepresented (w.r.t their natural abundance in the solar system) in cosmic ray particles. This is likely due to the comparably high ionization energy of both elements, which leads to less readily available hydrogen/helium ions. Since the acceleration mechanisms discussed in section 1.2 all couple to the net charge q of a particle, unionized hydrogen and helium are not accelerated [36].

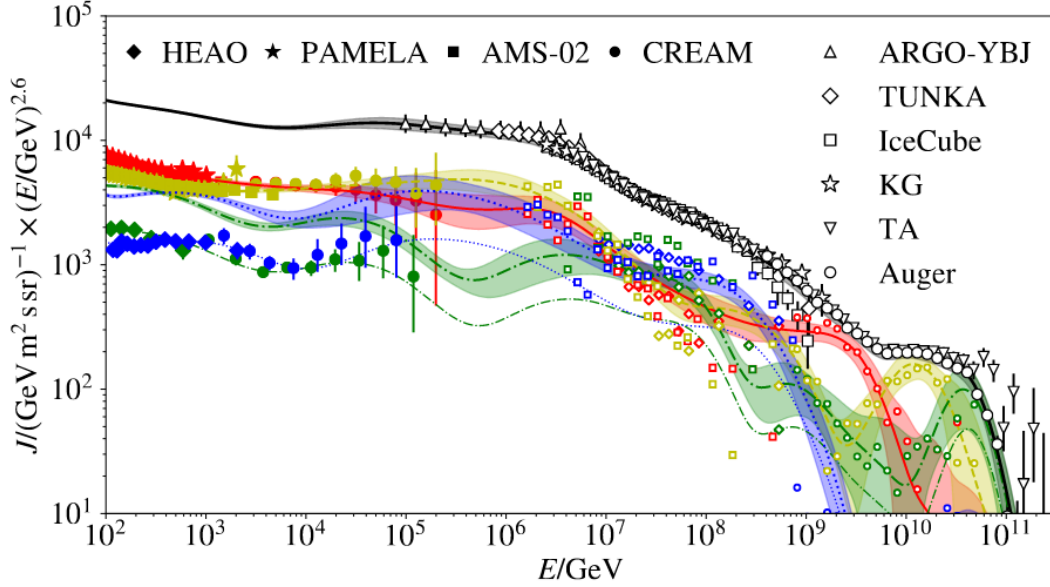


Figure 1.4: Measurements of the cosmic ray flux, multiplied by a factor $E^{2.6}$ for all types (black), and broken down by primary. Shown are protons (red), helium (yellow), oxygen (green) and iron (blue). Plot adopted from [39].

1.5 Energy spectrum

It has been discussed in section 1.2 that the expected CR flux w.r.t energy for supernova remnants is a powerlaw in the rough range of $200 \text{ MeV} < E \lesssim 100 \text{ TeV}$. Observations by various experiments extend this result to even higher energies. Their combined results are shown in Figure 1.4. However, while the general assumption of a powerlaw $\Phi(E) \propto E^\alpha$ holds over a large range of energies, kinks and other feature in the spectrum indicate that the spectral index α is not uniform, and instead a function of energy. The approximate form of $\alpha(E)$ will be discussed in the following by examining several key regions of the energy spectrum.

1.5.1 The proton knee $E \approx 10^{15} \text{ eV}$

Below an energy of $\approx 1 \text{ PeV} = 10^6 \text{ GeV}$, it is $\alpha(E) \approx 2.7$, while above a spectral index of $\alpha(E) \approx 3.0$ is found [38]. This softening of the spectrum (i.e. fewer particles of higher energy) could be attributed to several effects.

- **Dark matter channel** (partially falsified)

Weakly Interactive Massive Particles (WIMPs) are a popular candidate for Dark Matter (DM), as they correctly estimate the cosmological evolution of the universe [40]. A WIMP with a sufficiently high mass could explain the kink in the energy spectrum. CRs with $E > m_{\text{WIMP}} c^2$ could in theory produce DM in deeply-inelastic scattering processes. The degree of steepening in the spectrum is a measure

for how readily the process $X \rightarrow \text{WIMP} + Y$ occurs. The steeper the spectrum gets, the more particles are converted to DM, and the higher the corresponding cross sections are. Most theories involving WIMP creation can be excluded, since detectors at earthbound particle accelerators should have observed DM production at the observed steepening from 2.7 to 3.0 [41].

- **Escape during propagation**

While the analysis in subsection 1.3.1 concludes that the escape time for 10^{15} eV protons to leave their host galaxy is at least of the order 10^8 yr (compare Figure 1.2a), the calculations leading to this result are extremely simplified. If a more accurate treatment finds that particles with rigidities corresponding to the relevant energies are no longer confined by galactic magnetic fields, the kink could originate from particles leaving the milky way and not contributing to the flux observed on earth any longer.

- **Limited source energy**

A last possible explanation might lie in Equation 1.8. A prevalent acceleration mechanism for CRs below 10^{15} eV, such as shock acceleration in SNRs for example, might not be able to provide energies exceeding this threshold due to physical constraints. The spectrum above the proton knee is thus populated by CRs that originate from different acceleration mechanisms with different relations $\alpha(E)$.

1.5.2 The iron knee $E \approx 10^{17}$ eV

The spectrum exhibits various similar kinks at slightly higher energies than the one discussed in subsection 1.5.1, while it is assumed that they are ultimately caused by the same physical principles, each one corresponds to a different primary particle. Representatively, the iron knee at $E \approx 10^{17}$ eV is discussed here.

Because iron has both a higher mass and charge ($Z = 26$, $A = 56$) compared to the proton ($Z = A = 1$), different processes couple to the different nuclei with disparate strength. In particular, an iron core has a higher magnetic rigidity $R \propto \frac{A}{Z}$ than a proton of equivalent energy. This is explained by the fact that, while the iron core experiences a larger Lorentz force ($\propto Z$), the resulting acceleration ($\propto \frac{Z}{A}$) is not as strong due to a disproportionally larger mass ($\propto A$). It is thus logical to expect differences in the creation, propagation, and shower characteristics (see ?? for details) of different CR primary particles. By extension, the spectral index $\alpha(E)$ should be contrasting for each distinct particle type i , giving rise to different fluxes $\Phi(E)_i$, which is confirmed by Figure 1.4.

The ultimate cause of the different knees remains unknown currently. In the context of the ongoing AugerPrime upgrade, the Pierre Auger observatory will scan the energy spectrum at higher precision [42]. This will allow to test whether the location of the various kinks scale with A or with Z , and consequently shed light on the processes giving rise to these features.

1.5.3 The Ankle $E \approx 10^{18}$ eV

At an energy of roughly $\approx 1 \text{ EeV} = 10^9 \text{ GeV}$ an inflection point is found, where the spectrum hardens again from an index $\alpha(E) = 3.0$ to ≈ 2.7 . This might mark the final transition from predominantly galactic to intergalactic cosmic rays. If intergalactic CR sources such as AGNs have a harder spectrum (but lower luminosity) than galactic sources, the ankle could be well explained by a smooth transition from the latter to the former spectrum [43]. Other explanations focus on a change of the primary composition, which seems to be apparent in Figure 1.4 at the correct energy [44]. In any case, more data needs to be gathered to come to an informed conclusion on the ultimate cause.

1.5.4 The suppression $E \approx 10^{20}$ eV

At energies beyond 10^{20} eV a sharp drop in the flux can be noted. This represents the tail end of the spectrum, beyond which events are so rare that cosmic ray observatories can mostly just identify upper limits with their available statistics. The cause for the drop is actively debated, and might lie in the GZK cutoff discussed in subsection 1.3.2. Another explanation might be that the tail end represents the point at which even the largest and most powerful (in terms of energy) CR sources in the universe are not able to accelerate particles any further (c.f. Figure 1.1).

2 Extensive air showers

Consider a high energy cosmic ray impinging on earth. The questions pertaining to where it might originate from and how it has gained so much kinetic energy have been answered in the preceding sections. In the following, the particle cascades resulting from the particle interacting in the upper atmosphere will be examined. This is done in a two-fold way. The underlying principles will be explained via considering a particle carrying no SU(3)-color charge in section 2.1. The more general treatment for hadronic showers is then found in section 2.2. As supplementary information, the effect of different hadronic primaries is discussed in section 2.3.

2.1 Electromagnetic showers

The dominating interaction of $E > 10$ MeV photons in matter is e^+e^- pair production, whereas for electrons/positrons the creation of a γ via bremsstrahlung prevails at high energies. This is shown in Figure 2.1. Consequently, an entire cascade of electrons, positrons and photons can emerge from a single primary particle, as realised by Heitler in [47].

Of particular interest in these showers are, apart from the primary particles energy E_0 and arrival direction (Φ, θ) , the atmospheric depth X_{\max} at which it reaches its' maximum multiplicity, as well as the **Lateral Distribution Function** (LDF), that parametrizes the distribution of particles along the shower axis. An important variable that influences both values is the radiation length X_0 . It represents the characteristic length at which an e^\pm loses $1 - \frac{1}{e} \approx 63\%$ of its energy. It also corresponds to the mean free path of a photon in matter up to a factor $7/9$ [gupta2010calculation]. Neglecting said factor and assuming that, new particles on average inherit half of the original energy, describing the multitude of particles contained in an electromagnetic shower becomes a counting exercise in the context of the Heitler-model.

With each radiation length, the number of particles N in the shower double, while the energy per particle E_{pp} halves. After traversing an atmospheric depth of $n \cdot X_{\max}$, they consequently read

$$N(n) = 2^n, \quad E(n) = \frac{E_0}{2^n}. \quad (2.1)$$

After some time, the energy of each individual particle E_{pp} will have diminished by so much that other processes will dominate over bremsstrahlung and pair production. This occurs at the critical energy E_c below which the shower rapidly stops creating

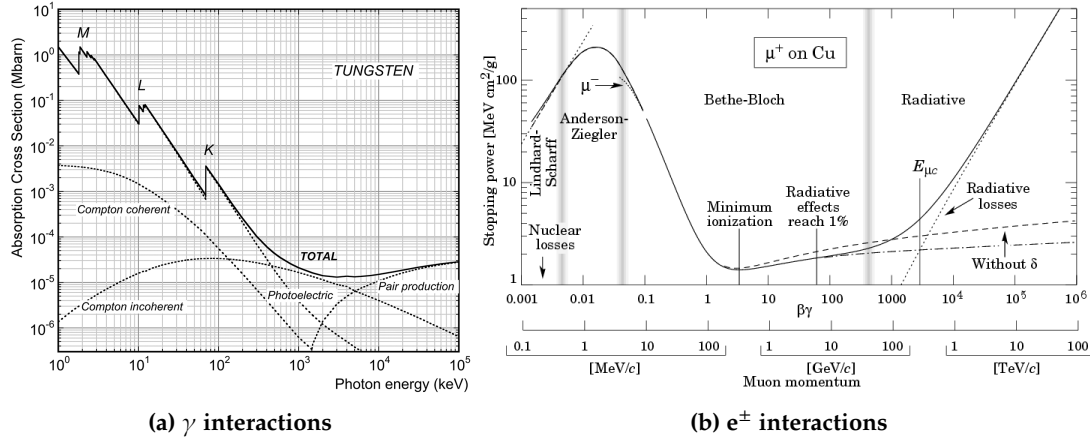


Figure 2.1: (a) Cross section for different energy loss processes of a photon in tungsten. The sudden spikes correspond to the transition energy of increasingly higher-energy electron shells. From [45]. (b) Stopping power of copper, representatively on an antimuon μ^+ , with respect to its' momentum. Plot adopted with changes from [46].

new particles and dies out as a result. It follows via Equation 2.2 and 2.3 that both X_{\max} as well as N_{\max} increase with E_0 . The multiplicity arising from these assumptions alongside a stylized propagation of the thus created shower is represented in Figure 2.2.

$$\begin{aligned}
 E_{PP}(n_{\max}) &\stackrel{!}{=} E_c \stackrel{(2.1)}{=} \frac{E_0}{2^{n_{\max}}} \\
 \Leftrightarrow \quad n_{\max} &= \lfloor \log_2 \left(\frac{E_0}{E_c} \right) \rfloor \\
 \Rightarrow \quad X_{\max} &= n_{\max} \cdot X_0 = \lfloor \log_2 \left(\frac{E_0}{E_c} \right) \rfloor \quad (2.2) \\
 \Rightarrow \quad N_{\max} &= 2^{n_{\max}} = \lfloor \frac{E_0}{E_c} \rfloor \quad (2.3)
 \end{aligned}$$

Lateral density function

2.2 Hadronic showers

Hadronic primaries will readily produce color-charged secondaries, as has been shown many times in particle accelerators. In order to model the development of hadronic showers, the model discussed in Equation 2.1 thus needs to be adjusted. An example theory has been developed by Heitler in [1]. Following the reasoning in [1], a hadronic primary creates N pions, of which half are charged, and half are uncharged (π^0). Their corresponding decay channels with the large **B** **R** **a** **n** **k** **i** **n** **g** **R** **a** **t** **i** **o** **s** (BR) are given below

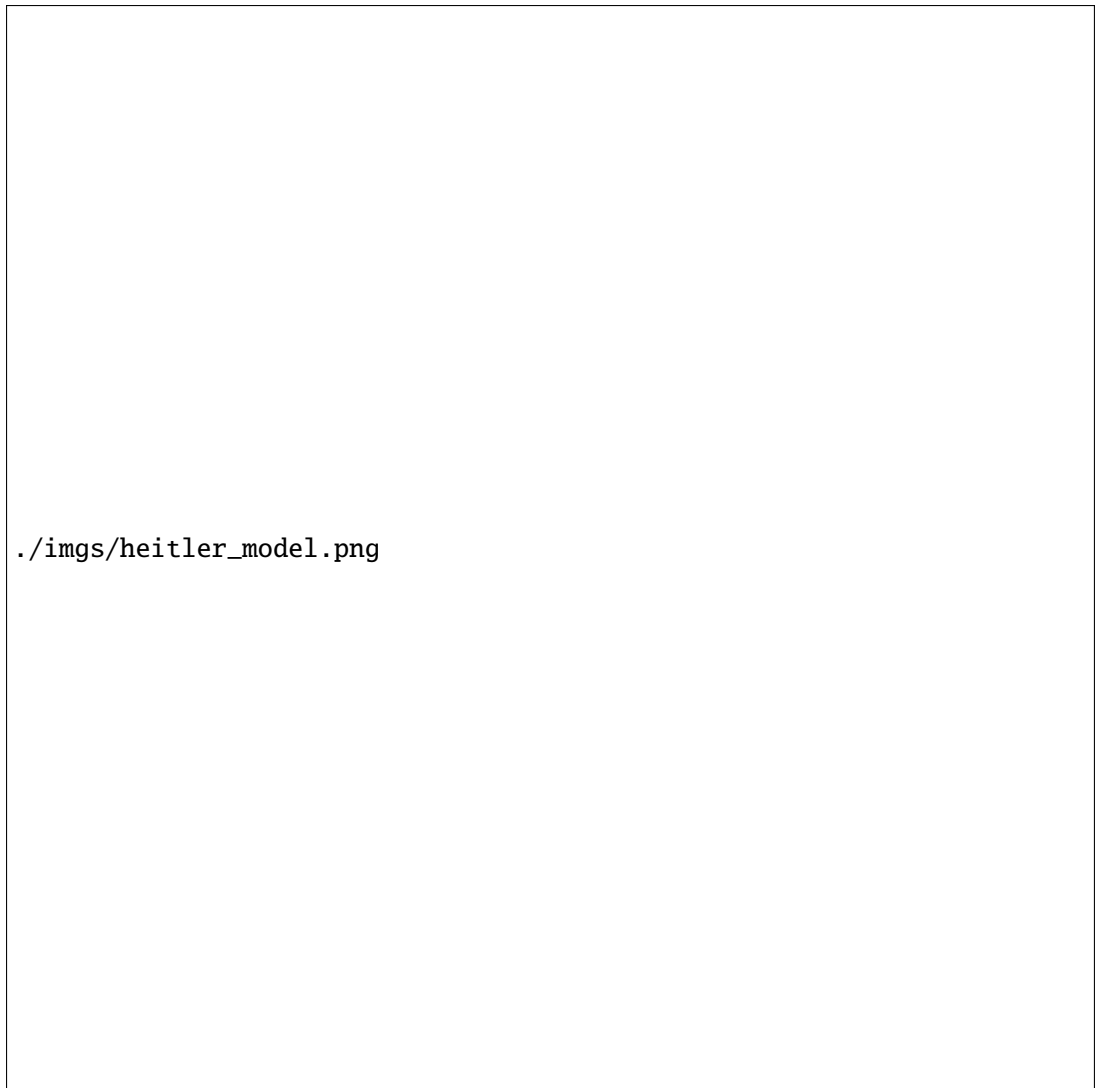


Figure 2.2: TODO

$$\pi^{\pm} \rightarrow \mu^{\pm} + \nu_{\mu}$$

$$\pi^0 \rightarrow 2\gamma$$

2.3 Superposition principle

3 The Pierre Auger Observatory

Located on the argentinian high-plains of Pampa Amarilla, the Pierre Auger observatory is a hybrid detector designed to detect and study cosmic rays of the highest energies. With an effective area of 3000 km^2 it is by far the largest experiment of its kind [48].

Although first proposed in 1992, it took 18 years until the idea of a large scale experiment to detect cosmic rays matured and construction of the first prototype started near Mendoza [49]. Some further 20 years later, the Pierre Auger collaboration has co-authored over publications and continues to advance research in astroparticle physics.

It does this via a hybrid approach, combining measurements of a **Surface Detector** (SD) as well as a **Flouresence Detector** (FD). Additional machinery, such as the **eXtreme** (XLF) and **Central Laser Facility** (CLF), is installed to monitor atmospheric variables. This improves the overall systematic accuracy of predictions made by the experiment. An overview of the site can be seen in Figure 3.1. Data measured by the FD, SD and the atmospheric monitors is sent to a **Central Data Acquisition System** (CDAS) located in the nearby town of Malargüe.

This chapter offers a brief look into the measurement principle and setup of the observatory. Information regarding the fluorescence detector can be found in section 3.1. The SD is described in section 3.2. A more in depth read on detector specifications and design choices is represented by the Pierre Auger observatory design report [48], where a lot of information stated in this chapter is conglomerated from. Notes on the event reconstruction are listed in section 3.3 and summarized from [50] and [51].

3.1 Fluorescence Detector (FD)

The FD consists of a total of 27 fluorescence telescopes (eyes) at 4 different sites. Each eye monitors a $30^\circ \times 30^\circ$ window of the sky at a resolution of $\approx 0.5 \frac{\text{px}}{\text{deg}^2}$. This results in an effective FOV of roughly $180^\circ \times 30^\circ$ per FD station, with an exception of Coihueco, where three additional telescopes - HEAT (**H**igh **E**levation **A**uger **T**elescope) - are installed to enable monitoring of higher zenith angles ($30^\circ \leq \theta \leq 60^\circ$) and increase sensitivity for showers of lower energies (compare chapter 1). A schematic of the setup of each eye is given in Figure 3.2a.

The individual telescopes consist of 3.6 m by 3.6 m, convex mirrors. They reflect incoming light onto a set of 440 photomultipliers (PMTs), each corresponding to one pixel in the resulting image seen by an eye. Since the setup needs to be extremely sensitive to UV light in order to detect flouresence caused by extensive air showers, its operation is limited to the relatively noise free moonless astronomical nights (Sun

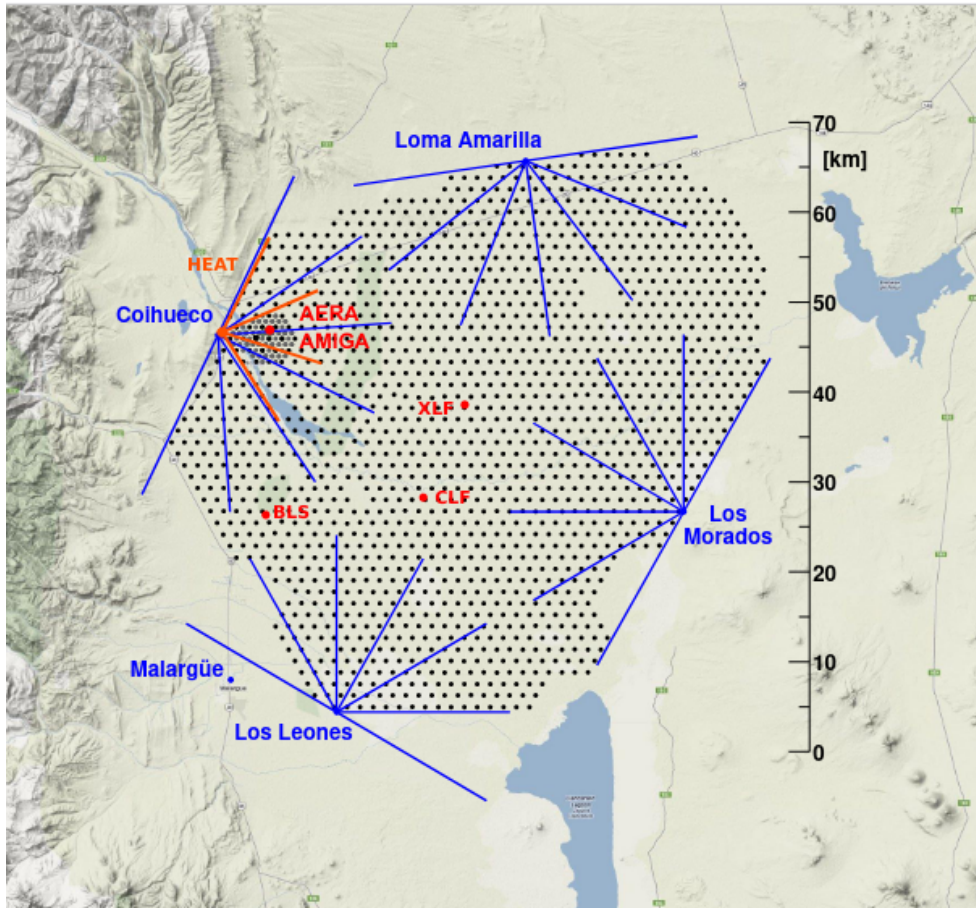


Figure 3.1: Overview of the Pierre Auger observatory. The four different FD sites (respective FOV shown with blue lines) sit at the edge of the detector area and monitor the night sky above the SD array consisting of 1600 water tanks (black dots). A denser spacing of stations near Colihueco is equipped with additional electronics such as e.g. radio antennas (AERA) and muon detectors (AMIGA). Image taken from [52]

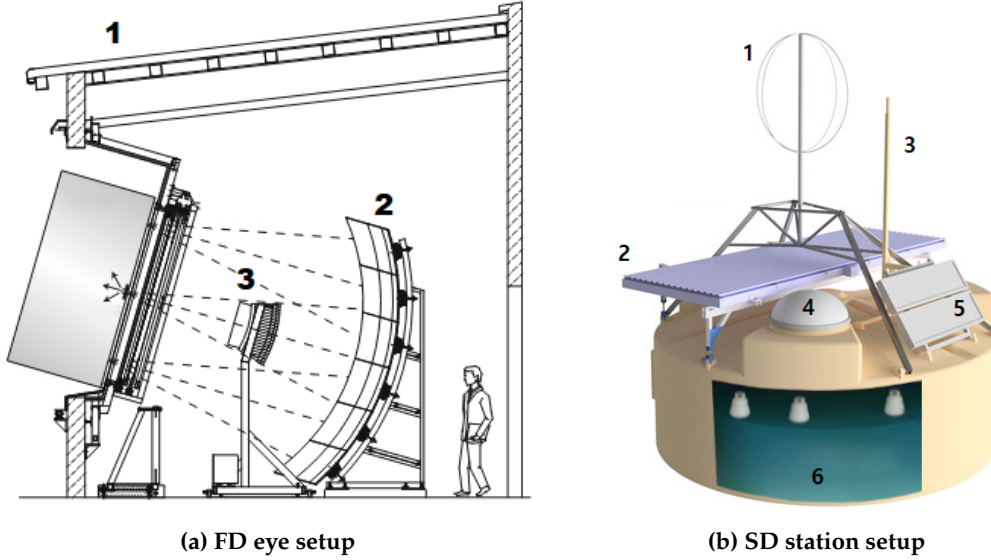


Figure 3.2: (a) Schematic view of an FD eye with housing (1), main mirror (2) and camera (3). Image taken from [51] (b) Setup of an SD WCD with radio antenna (1), SSD (2), communication and GPS antenna (3), electronics box (4), solar panels (5) and the WCD (6). Image adopted with changes from [53] and [54]

$\angle \text{Horizon} \lesssim -18^\circ$). When the FD is operational, this allows the observation of the longitudinal propagation of a shower instead of just its' footprint (as seen by the SD).

3.2 Surface Detector (SD)

The SD consists of 1600 individually operating stations, spaced apart on a hexagonal grid with a standard 1.5 km spacing. Each station is made up of a main tank filled with 12 000 L of purified water and reflective inner walls, a solar panel and batteries for power management, as well as an antenna for communication. Within each tank three PMTs detect Cherenkov light originating from shower particles, these are together with the tank referred to as **Water Cherenkov Detectors (WCDs)**. With the (at the time of this work) ongoing AugerPrime upgrade, each station is additionally equipped with a small **PMT (sPMT)**, **Surface Scintillator Detector (SSD)**, and radio antenna atop the tank. This allows for the recording of stronger signals, finer separation of electromagnetic and muonic shower component and detection of highly inclined air showers respectively [55, 56]. Figure 3.2b shows a schematic blueprint of each SD station.

3.2.1 Data acquisition (DAQ)

Onboard electronics, the **Upgraded Unified Board (UUB)**, or more precisely six 10-bit **Flash Analog-to-Digital-Converters (FADCs)** read out measurement data from the PMTs at a sampling rate of 120 MHz (≈ 8.33 ns binning) [57]. This is done in a two-fold

way. Three FADCs digitize the PMTs dynode voltage, resulting in the **High Gain** (HG) output. Three FADCs monitor the anode voltage to form the **Low Gain** (LG) output, which can be analyzed if the HG output exceeds a value of 2^{10} ADC counts and becomes saturated. This effectively enables the measurement of both large ($\geq O(10^3)$ particles hitting the tank) as well as small shower signals ($O(1)$ particle hitting the tank) with sufficient accuracy [50]. Once an FADC bin has been recorded and checked for possible triggers (c.f. ??) it is written to a ring buffer. If a trigger is issued, the corresponding chunk in the ring buffer ($\approx 4.992 \mu\text{s}$ (599 bins) before and $12.07 \mu\text{s}$ (1448 bins) after a trigger, $2047 + 1$ bins total), the measured trace, can be analyzed in order to calibrate a station in the array (subsection 3.2.3, subsection 3.2.2) or processed by a higher-level CPU for event reconstruction purposes (see section 3.3).

While each station is equipped with the same electronics and runs the same analysis software, variables like the position in the field, station age or slight changes in the manufacturing/installation process cause different stations to age differently. Over the lifetime of the array such differences can sum into potentially drastic discrepancies in gathered data. Put simply, an extensive air shower will look different both to different WCDs at the same time as well as the same WCD at different times. To account for this, measurements are standardized across all stations. ADC counts are related to a **Vertical Equivalent of through-going Muons** (VEM) that would result in the same signal strength. In this fashion, the maximum response that is generated by a PMT from one vertically through-going muon is defined as $1 \text{ VEM}_{\text{Peak}}$. The total deposited charge (equivalent to the integral of the response) is defined as $1 \text{ VEM}_{\text{Ch.}}$. The conversion factor between ADC counts and VEM_{Peak} and $\text{VEM}_{\text{Ch.}}$ (referred to as I_{Peak} and Q_{Peak} respectively) is estimated from data and continuously updated separately for each station. Note that due to the limited computational resources of the WCD, as well as constraints on the amount of data that can be transmitted per station in the SD array ($1200 \frac{\text{bit}}{\text{s}}$, [58]), a simplified, rate-based approach is implemented for autonomous calibration in the field (Online calibration), this stands in contrast to the more physics-driven histogram method used during event reconstruction (Offline calibration). In any case, both algorithms are listed in the following subsections and discussed in more detail in the referenced literature.

3.2.2 Offline calibration

Baseline estimation

In order to estimate I_{Peak} and Q_{Peak} of a WCD tank first the baseline - the average response in the absence of any signals - of each PMT needs to be determined. All further analysis will then be based on the baseline-subtracted PMT data.

For event reconstruction, a first baseline estimate of a WCD PMT is predicted by examining the beginning and end of a 2048 bin ($17.06 \mu\text{s}$) long trace. The mode m as well as standard deviation σ of the first (last) 300 bins is calculated. All bins larger or smaller than $m \pm 2\sigma$ are truncated and removed from the trace window. The value of m , σ is consequently updated and the procedure repeated until a convergence is

reached and no further cut is necessary. The best estimate B_{front} (B_{end}) for the front (end) of the trace at this point is given by the mean value of all remaining bins. It's statistic uncertainty $\sigma_{B_{\text{front}}}$ ($\sigma_{B_{\text{end}}}$) is given by the standard deviation of the remaining bins [59]. The baseline between the flat front and end estimate is then interpolated based on the difference

$$\Delta B = B_{\text{end}} - B_{\text{front}}. \quad (3.1)$$

- **Rejection of anomalous upward fluctuations $\frac{\Delta B}{\sigma_{\Delta B}} \geq +10$:**

B_{end} being higher than B_{front} often indicates errors in the electronic readout or defect components in the measurement chain. There exists no physical reason why the end baseline should be (significantly) higher than the front. Consequently, traces where this is the case are ignored during event reconstruction.

- **Constant approximation for small upward fluctuations $+5 > \frac{\Delta B}{\sigma_{\Delta B}} \geq 0$:**

Small fluctuations of the baseline are expected and the norm. If these fluctuations are positive ($B_{\text{end}} > B_{\text{front}}$) the method of calculating the mode, truncating outliers and repeating both steps is applied to the entire length of the signal, resulting in a constant baseline estimate B across the trace.

- **Step-function approximation for small downward fluctuations $0 > \frac{\Delta B}{\sigma_{\Delta B}} \geq -1$:**

Unlike positive fluctuations, negative fluctuations ($B_{\text{end}} < B_{\text{front}}$) can have a physical significance. Due to the undershoot of PMTs after detecting a signal in the WCD (compare [glietta2008recovery]), the baseline estimate decreasing towards the end of the trace often indicates the presence of shower particles within the tank. For this reason, downward fluctuations are handled differently from upward ones. If the fluctuations are sufficiently small, the baseline across the trace is estimated as a simple step-function; The trace is separated into two parts along its' maximum ADC value. The front part (i.e. before the max. value) has the baseline B_{front} , while the rear part is estimated by B_{end} . An example of this is shown in Figure 3.3a.

- **Charge-linear approximation for large undershoots $-1 \geq \frac{\Delta B}{\sigma_{\Delta B}}$:**

For larger undershoots, the baseline is estimated bin by bin based on the deposited charge in the detector. Starting with a value of B_{front} for the bins 1-300, the remaining baseline is first linearly interpolated according to Equation 3.2,

$$b_i = B_{\text{front}} - \Delta B \cdot \frac{i - 300}{1448}, \quad 300 \leq i \leq 2048, \quad (3.2)$$

where the magic numbers 300 and 1448 refer to the last bin of the front baseline estimate and the length of the interpolated baseline respectively. From this, the deposited charge q_i up to bin i can be calculated as per Equation 3.3.

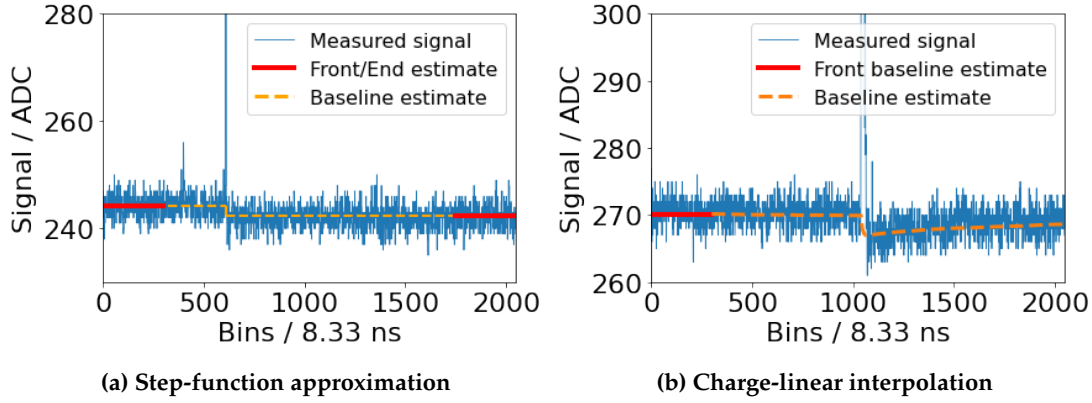


Figure 3.3: (a) A simple step function is sufficient to accurately model a PMTs' noise level at small downward fluctuations. (b) For larger discrepancies the more involved charge-linear interpolation is used. Note that the signal undershoot is exaggerated for visualization purposes in both examples.

$$q_i = \sum_{k=0}^i (T_k - b_k) \exp\left(-\frac{8.33 \text{ ns}}{\tau} \cdot (i - k)\right) \quad (3.3)$$

In Equation 3.3, T_k refers to the numerical value of bin k . Note that an exponential falloff term has to be added to account for the decay in signal undershoot with a decay time of $\tau = 45 \mu\text{s}$. The value of τ is determined in [60]. Assuming the magnitude of the signal undershoot is directly proportional to the deposited charge q , a correction of the baseline thus becomes

$$b_i = B_{\text{front}} + \frac{q_i}{q_{1898}} \cdot \Delta B. \quad (3.4)$$

The parametrization in Equation 3.4 is chosen such that the charge-interpolated baseline at bin 1898 (the center position in the last 300 bins) is exactly equal to the rear baseline estimate B_{end} . The prediction can be made more accurate by repeating the above steps, each time recalculating q_i and readjusting the baseline b_i in the process. Figure 3.3b shows an example baseline estimate after three such iterations. In general, it converges to a robust estimate within five repetitions [60].

Estimation of I_{Peak} and Q_{Peak}

The conversion factor between ADC counts and VEM_{Peak} , VEM_{Ch} are built from distributions of traces that satisfy the muon trigger, which scans incoming ADC bins for a value exceeding the muon threshold $t_{\mu} = b + 30 \text{ ADC}$, 30 ADC above baseline, for any of the three WCD PMTs. If this requirement is met, 69 bins (19 before, trigger bin, 49 after) are written to the muon buffer, a FIFO (first-in-first-out) type memory storage,

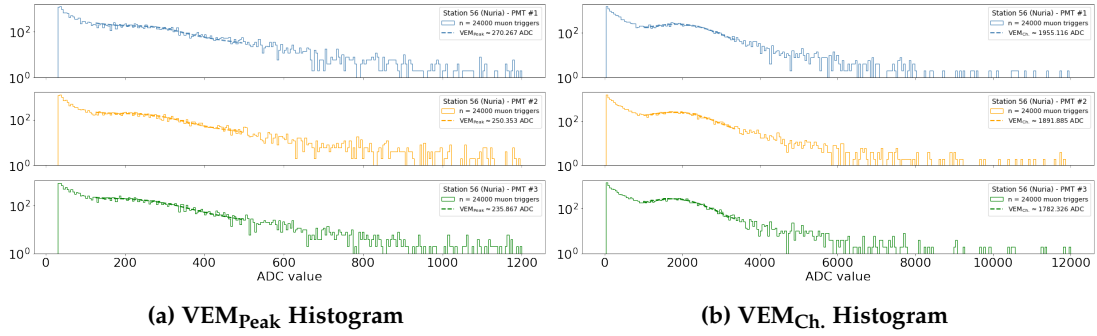


Figure 3.4: (a) The maximum value of each muon trace is histogrammed in order to gain information about the current value of I_{Peak} of a station. (b) The conversion factor from recorded ADC values to Q_{Peak} is given from the histogrammed sum of each muon trace.

that is subsequently filled with low-energy events, which (in general) didn't satisfy any other trigger but still contain useful information [58].

By histogramming the maximum value (sum) of each trace, the plot shown in Figure 3.4a (Figure 3.4b) can be obtained. It becomes apparent that the number of events per bin largely follows a power law with negative spectral index. This is expected considering the discussion in chapter 1. Notable are characteristic deviations from this powerlaw, as these contain information about I_{Peak} and Q_{Peak} :

- Low energy events from e.g. e^- , e^+ that deposit their entire energy in the tank give rise to a surplus of events at lower ADC values.
- A characteristic (muon) hump appears in the bins 20–70. This surplus is caused by omni-directional muons impinging onto the detector. Since the energy deposited by such muons is roughly constant, the center of the muon hump serves as an estimate of I_{Peak} (Q_{Peak}).
- (Not depicted in Figure 3.6) In similar plots from related works (c.f. [58, 61]) a drastic increase in bin occupations towards the tail end of the histograms can be observed. This is attributed to an increased bin size from 1500 ADC counts onwards, which reduces the amount of data per station sent to CDAS. In the example plots referenced here, a constant binning is chosen instead. This difference is mentioned here to avoid possible confusion.

In this fashion, the average response of the WCD to a through-going muon can be estimated by e.g. fitting a gaussian distribution to the muon hump. However, there exists a systematic difference between the response to a vertical or an omni-directional muon. Consequently, correctional factors need to be applied to the analysis results. These have been determined in previous experiments [62]. Finally, one arrives at an estimate for the conversion factor between ADC counts and VEM_{Peak} , $\text{VEM}_{\text{Ch.}}$.

3.2.3 Online calibration

Baseline estimation

Each SD station has an autonomous estimate of its' three WCD PMT baselines. They are defined simply as the mean of all first bins for each trace contained in the respective muon buffers (see subsection 3.2.3). This baseline estimate is used to set the thresholds of the hardware triggers discussed in ??.

Estimation of I_{Peak} and Q_{Peak}

Due to the limited computational resources in each station, the determination of I_{Peak} and Q_{Peak} at station-level is fairly naive. Nevertheless, the σ - δ -method shown here has proven to be incredibly robust over the lifetime of the SD array [48].

In the beginning, the to-be-estimated value $I_{\text{Peak}}^{\text{est.}}$ ($Q_{\text{Peak}}^{\text{est.}}$) is set to the same, predefined value for all PMTs. A simple single-bin calibration trigger requiring all available WCD PMTs to be above a threshold of $t_{70} = 1.75 I_{\text{Peak}}^{\text{est.}}$ above baseline plus a given PMT exceeding $2.5 I_{\text{Peak}}^{\text{est.}}$ is used to determine a calibration trigger rate. If for some reason not all three WCD PMTs are functional, the thresholds are altered according to Table 3.1. What follows is an iterative procedure to approximate I_{Peak} (Q_{Peak}):

1. Calculate the trigger rate $r_{\text{cal.}}$ of the calibration trigger over a time $t_{\text{cal.}} = 5$ s.
2. Adjust $I_{\text{Peak}}^{\text{est.}}$ ($Q_{\text{Peak}}^{\text{est.}}$) by $\pm\delta$ if $\pm(r_{\text{cal.}} - 70 \text{ Hz}) \geq 2 \text{ Hz}$, with $\delta = 1 \text{ ADC}$ initially.
3. If $t_{\text{cal.}} < 60$ s increase $t_{\text{cal.}}$ by 5 s. If $\delta > 0.1 \text{ ADC}$ decrease δ by 0.1 ADC.
4. While $t_{\text{cal.}} < 60$ s jump to step 1, else return $I_{\text{Peak}}^{\text{est.}}$ ($Q_{\text{Peak}}^{\text{est.}}$).

Table 3.1

n_{PMT}	t_{70}
1	2.85
2	2.00
3	1.75

3.3 Event Reconstruction

If an event has been detected (subsection 3.3.1) it is reconstructed at CDAS level, where information from all relevant detectors is conglomerated. From the observed shower footprint in the SD array as well as the (if available) longitudinal profile measured by the FD stations follows an estimate on arrival direction (subsection 3.3.3), energy

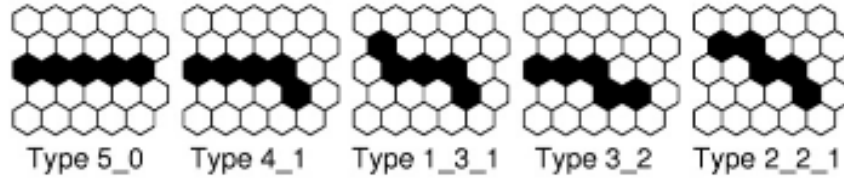


Figure 3.5: Fundamental shape of tracks considered straight. Image from [51].

(subsection 3.3.4) and primary particle (subsection 3.3.5). As the work presented in this thesis solely deals with the surface detector of the Auger observatory, this section focuses heavily on the SD reconstruction. Addendums towards FD reconstruction are given where needed.

3.3.1 Trigger procedure

The flux of cosmic rays especially at the highest energies is barely of the order of $1 \text{ km}^{-2} \text{ yr}^{-1}$ [19]. Consequently, most signals observed by the Auger observatory stem from low-energy cosmic muons and not extensive air showers. This is reflected in the hierarchical structure of the triggers, which effectively reject such events. The overall event detection is split up into three tiers, T1, T2 and T3, where T3 implies the detection of an extensive air shower by either the FD or the SD (or both).

T1 trigger

T1 level triggers are implemented at the lowest possible level. This means each FD eye or each SD station raises T1 triggers autonomously. They serve as a first indicator on whether or not a signal of any kind is present. For the most part, this is realised by checking for elevated signal strengths, i.e. for hot pixels in a FD telescopes image or PMT outputs of an SD station that are significantly above baseline. The respective trigger thresholds are calibrated such that the nominal trigger rate during operation is roughly 100 Hz [51, 50].

T2 trigger

T2 level triggers occur at the same location as T1-type triggers. They are different in their more stringent conditions on the signal size or shape. This for example entails track shape identification for the FD telescopes, where straight tracks (see Figure 3.5) of hot pixels are identified. If the resulting pixel track passes an additional quality cut that rejects e.g. lightning signals, the T2 is directly promoted to a T3 trigger (= Event). For the SD, an exact discussion of T2 triggers is given in ???. A single tank on average records T2-type events at a rate of 20 Hz and forwards this information to the CDAS along with a timestamp. There, incoming information of all tanks is scanned for spatial and temporal correlations, which indicate the presence of an extensive air shower.

T3 trigger

T3 type triggers, or event type triggers are (with the exception of FD events, which have been discussed above) built from distributions of at least three SD stations next to each other that recorded a T2 trigger in close temporal succession. Upon the detection of such a pattern a readout command is issued to all nearby stations. Their recorded FADC traces as well as calibration information are forwarded to CDAS if the station observed a T1/T2 event within an appropriate timespan of order $O(\mu\text{s})$ before or after the T3 pattern occurrence. Such a modus operandi enables an accurate reconstruction of the shower footprint by including stations that did not participate in the initial T3 trigger. This extends to FD issued T3 triggers, where potential information from SD stations in the vicinity of the FD-reconstructed shower core position is requested.

3.3.2 Core position

All reconstruction algorithms presented in the following subsections rely in one form or the other on an accurate determination of where the shower was recorded above the observatory. Hence the center of the shower footprint, the shower core, must be estimated at the beginning of the analysis chain.

Without any prior knowledge, a first guess as to where the shower core is located can be made by calculating the barycenter of all participating stations. In this fashion, a weighted mean of all station locations is constructed weights equal to the square root of the corresponding signal strength [50].

The presented approach fails if only parts of the shower are contained within the SD event. This occurs espically at the edges of the SD array, or in the vicinity of faulty WCDs. A fiducial trigger, NT5 is employed to mitigate this problem. NT5 requires at least N active stations around the SD detector that recorded the largest signal [63].

3.3.3 Arrival direction

The shower footprint measured by the SD (example given in Figure 3.6a) corresponds to the projection of the shower plane onto the detector plane, i.e. the ground. It can be assumed that the shower plane has a fixed (hyperbolic [64]) shape and propagates at the speed of light along the primary particles trajectory. With this knowledge, estimating the arrival direction becomes a task of minimizing the difference between measured and expected arrival times given by an example shower axis anchored at the reconstructed shower core. The axis for which the summed differences is minimal corresponds to the most likely arrival direction of the primary particle.

Naturally, the expected variance on the reconstructed ϕ and θ diminishes the more stations participate in the combined fit. The angular resolution thus decreases for larger energies of the primary particle. This can be seen in Figure 3.6b. In any case, the angular resolution even at smaller energies is better than 2.2° . For hybrid events,

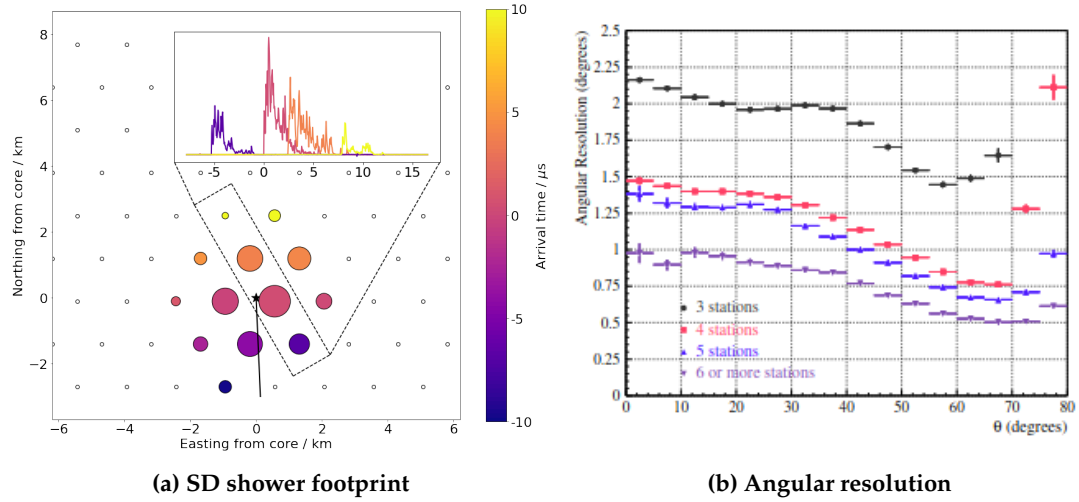


Figure 3.6: (a) An example shower footprint recorded by the individual SD tanks (circles). The measured signal strength and arrival time is encoded in the size and color for each station. Tanks that haven't recorded any signal are shown colorless. For a subset of stations the respective VEM trace and consequently the propagation of the signal in the SD detector is shown in the inset plot on the top right. (b) The angular resolution as a function of θ for energies exceeding 3 EeV. Image from [64].

where the shower has also been detected by the FD, the angular resolution is greatly increased to about 0.6° [64].

3.3.4 Energy estimation

After a shower core has been pinpointed and the shower axis was determined, all information to fit an LDF is present. The ShowerPlane distance (SPD), the minimal separation between shower axis and station position, is calculated for each tank participating in the event and related to the integrated signal (in units of) it received. From the so gathered lateral distribution of a shower the integrated signal $S(1000)$ of a hypothetical (labelled dense) station laying at $\text{SPD} = 1000 \text{ m}$ is obtained.

3.3.5 Primary particle

Bibliography

- [1] Robert A Millikan and G Harvey Cameron. "The origin of the cosmic rays". In: *Physical review* 32.4 (1928), p. 533.
- [2] Thomas H Johnson. "A note on the nature of the primary cosmic radiation". In: *Physical Review* 54.5 (1938), p. 385.
- [3] Nobel Media AB. *Press release*. <https://www.nobelprize.org/prizes/physics/1936/summary/>. Accessed: 18th Jul. 2022. 1936.
- [4] Pierre Auger et al. "Extensive cosmic-ray showers". In: *Reviews of modern physics* 11.3-4 (1939), p. 288.
- [5] Sergey Ostapchenko. "Status of QGSJET". In: *AIP Conference Proceedings*. Vol. 928. 1. American Institute of Physics. 2007, pp. 118–125.
- [6] I Goldman et al. "Implications of the supernova SN1987A neutrino signals". In: *Physical review letters* 60.18 (1988), p. 1789.
- [7] J Abraham et al. "Measurement of the energy spectrum of cosmic rays above 1018 eV using the Pierre Auger Observatory". In: *Physics Letters B* 685.4-5 (2010), pp. 239–246.
- [8] Alexander Aab et al. "Searches for anisotropies in the arrival directions of the highest energy cosmic rays detected by the Pierre Auger Observatory". In: *The Astrophysical Journal* 804.1 (2015), p. 15.
- [9] Hannes Alfvén. "Existence of electromagnetic-hydrodynamic waves". In: *Nature* 150.3805 (1942), pp. 405–406.
- [10] Enrico Fermi. "On the origin of the cosmic radiation". In: *Physical review* 75.8 (1949), p. 1169.
- [11] AM Hillas. "Can diffusive shock acceleration in supernova remnants account for high-energy galactic cosmic rays?" In: *Journal of Physics G: Nuclear and Particle Physics* 31.5 (2005), R95.
- [12] Pasquale Blasi. "The origin of galactic cosmic rays". In: *The Astronomy and Astrophysics Review* 21.1 (2013), pp. 1–73.
- [13] Katsuaki Asano and Masaaki Hayashida. "The most intensive gamma-ray flare of quasar 3C 279 with the second-order Fermi acceleration". In: *The Astrophysical Journal Letters* 808.1 (2015), p. L18.
- [14] Ruth A Daly. "Black hole spin and accretion disk magnetic field strength estimates for more than 750 active galactic nuclei and multiple galactic black holes". In: *The Astrophysical Journal* 886.1 (2019), p. 37.

-
- [15] Elliott Flowers and Malvin A Ruderman. "Evolution of pulsar magnetic fields". In: *The Astrophysical Journal* 215 (1977), pp. 302–310.
 - [16] FM Rieger and K Mannheim. "Particle acceleration by rotating magnetospheres in active galactic nuclei". In: *arXiv preprint astro-ph/9911082* (1999).
 - [17] Zaza Osmanov, Andria Rogava, and Gianluigi Bodo. "On the efficiency of particle acceleration by rotating magnetospheres in AGN". In: *Astronomy & Astrophysics* 470.2 (2007), pp. 395–400.
 - [18] Frank M Rieger. "Cosmic ray acceleration in active galactic nuclei-on centaurus a as a possible uhedr source". In: *arXiv preprint arXiv:0911.4004* (2009).
 - [19] Anthony M Hillas. "The origin of ultra-high-energy cosmic rays". In: *Annual review of astronomy and astrophysics* 22 (1984), pp. 425–444.
 - [20] AU Abeysekara et al. "Very-high-energy particle acceleration powered by the jets of the microquasar SS 433". In: *Nature* 562.7725 (2018), pp. 82–85.
 - [21] Aya Ishihara, IceCube Collaboration, et al. "Extremely high energy neutrinos in six years of IceCube data". In: *Journal of Physics: Conference Series*. Vol. 718. 6. IOP Publishing. 2016, p. 062027.
 - [22] Frank C Jones. "Inverse Compton scattering of cosmic-ray electrons". In: *Physical Review* 137.5B (1965), B1306.
 - [23] Enrico Fermi. "98. Galactic Magnetic Fields and the Origin of Cosmic Radiation". In: *A Source Book in Astronomy and Astrophysics, 1900–1975*. Harvard University Press, 2013, pp. 671–676.
 - [24] Matthias Bartelmann. "Gravitational lensing". In: *Classical and Quantum Gravity* 27.23 (2010), p. 233001.
 - [25] Matthias Bartelmann and Peter Schneider. "Weak gravitational lensing". In: *Physics Reports* 340.4-5 (2001), pp. 291–472.
 - [26] Marijke Haverkorn. "Magnetic fields in the Milky Way". In: *Magnetic fields in diffuse media*. Springer, 2015, pp. 483–506.
 - [27] Pierre Auger Collaboration et al. "Observation of a large-scale anisotropy in the arrival directions of cosmic rays above 8×10^{18} eV". In: *Science* 357.6357 (2017), pp. 1266–1270.
 - [28] J Skilling. "The diffusion of cosmic rays". In: *Monthly Notices of the Royal Astronomical Society* 147.1 (1970), pp. 1–12.
 - [29] Leonard Searle and Robert Zinn. "Compositions of halo clusters and the formation of the galactic halo". In: *The Astrophysical Journal* 225 (1978), pp. 357–379.
 - [30] Particle Data Group et al. "Review of Particle Physics". In: *Progress of Theoretical and Experimental Physics* 2020.8 (Aug. 2020). 083C01. ISSN: 2050-3911. DOI: 10.1093/ptep/ptaa104. eprint: <https://academic.oup.com/ptep/article-pdf/2020/8/083C01/34673722/ptaa104.pdf>. URL: <https://doi.org/10.1093/ptep/ptaa104>.
 - [31] Kenneth Greisen. "End to the cosmic-ray spectrum?" In: *Physical Review Letters* 16.17 (1966), p. 748.

- [32] GT Zatsepin and VA Kuz'min. "J. of Exp. and Theor". In: *Phys. Lett* 4 (1966), p. 78.
- [33] Vadim N Gamezo, Alexei M Khokhlov, and Elaine S Oran. "Three-dimensional delayed-detonation model of type Ia supernovae". In: *The Astrophysical Journal* 623.1 (2005), p. 337.
- [34] John J Cowan and Friedrich-Karl Thielemann. "R-process nucleosynthesis in supernovae". In: *Physics Today* 57.10 (2004), pp. 47–54.
- [35] M Garcia-Munoz, GM Mason, and JA Simpson. "The age of the galactic cosmic rays derived from the abundance of Be-10". In: *The Astrophysical Journal* 217 (1977), pp. 859–877.
- [36] JZ Wang et al. "Measurement of cosmic-ray hydrogen and helium and their isotopic composition with the BESS experiment". In: *The Astrophysical Journal* 564.1 (2002), p. 244.
- [37] Michael W Kirson. "Mutual influence of terms in a semi-empirical mass formula". In: *Nuclear Physics A* 798.1-2 (2008), pp. 29–60.
- [38] Thomas K Gaisser, Ralph Engel, and Elisa Resconi. *Cosmic rays and particle physics*. Cambridge University Press, 2016.
- [39] Hans Dembinski et al. "Data-driven model of the cosmic-ray flux and mass composition from 10 GeV to 10^{11} GeV". In: *arXiv preprint arXiv:1711.11432* (2017).
- [40] Anatoly Klypin et al. "Structure formation with cold+ hot dark matter". In: *arXiv preprint astro-ph/9305011* (1993).
- [41] Fiorenza Donato et al. "Constraints on WIMP Dark Matter from the High Energy PAMELA p/p data". In: *Physical review letters* 102.7 (2009), p. 071301.
- [42] Antonella Castellina. "AugerPrime: the Pierre Auger observatory upgrade". In: *EPJ Web of Conferences*. Vol. 210. EDP Sciences. 2019, p. 06002.
- [43] Roberto Aloisio et al. "A dip in the UHECR spectrum and the transition from galactic to extragalactic cosmic rays". In: *Astroparticle Physics* 27.1 (2007), pp. 76–91.
- [44] Denis Allard. "Extragalactic propagation of ultrahigh energy cosmic-rays". In: *Astroparticle Physics* 39 (2012), pp. 33–43.
- [45] Sow-Hsin Chen and Michael Kotlarchyk. *Interactions of photons and neutrons with matter*. World Scientific, 2007.
- [46] Stefano Meroli. "The Straggling function. Energy Loss Distribution of charged particles in silicon layers". In: *Home Cern*, https://meroli.web.cern.ch/lecture_-StragglingFunction.html (2017).
- [47] Walter Heitler. *The quantum theory of radiation*. Courier Corporation, 1984.
- [48] Alexander Aab et al. "The pierre auger observatory upgrade-preliminary design report". In: *arXiv preprint arXiv:1604.03637* (2016).
- [49] The Pierre Auger Collaboration. *Timeline of the Pierre Auger Observatory*. <https://auger.org/observatory/timeline-observatory>. Accessed: 04th Oct. 2022. 2022.

- [50] Alexander Aab et al. "Reconstruction of events recorded with the surface detector of the Pierre Auger Observatory". In: *Journal of Instrumentation* 15.10 (2020), P10021.
- [51] Jorge Abraham et al. "The fluorescence detector of the Pierre Auger Observatory". In: *Nuclear Instruments and Methods in Physics Research Section A: Accelerators, Spectrometers, Detectors and Associated Equipment* 620.2-3 (2010), pp. 227–251.
- [52] Darko Veberič. *Auger array*. https://web.ikp.kit.edu/darko/auger/auger-array/auger_array-pdf/auger_array-ad.pdf. Accessed: 19th Jul. 2022. 2021.
- [53] The Pierre Auger Collaboration. *AugerPrime*. <https://auger.org/observatory/augerprime>. Accessed: 06th Nov. 2022.
- [54] João de Mello Neto, ed. *Physics and astrophysics of ultra-high energy cosmic rays: recent results from the Pierre Auger Observatory*. NUCLEUS - 2020.
- [55] Antonella Castellina. "AugerPrime: the Pierre Auger observatory upgrade". In: *EPJ Web of Conferences*. Vol. 210. EDP Sciences. 2019, p. 06002.
- [56] Jörg R Hörandel. "Precision measurements of cosmic rays up to the highest energies with a large radio array at the Pierre Auger Observatory". In: *EPJ Web of Conferences*. Vol. 210. EDP Sciences. 2019, p. 06005.
- [57] Valerio Verzi et al. "The energy scale of the Pierre Auger Observatory". In: *Proceedings of the 33rd ICRC, Rio de Janeiro, Brasil* (2013).
- [58] Xavier Bertou et al. "Local-Station Calibration". GAP 2022-0??
- [59] Tobias Schulz et al. "New Baseline Algorithm for UB Traces". GAP 2022-045.
- [60] Tobias Schulz et al. "New Baseline Algorithm for UUB Traces". GAP 2022-0??
- [61] Alexander Streich et al. "Performance of the upgraded surface detector stations of the Pierre Auger Observatory". In: *Verhandlungen der Deutschen Physikalischen Gesellschaft* (2018).
- [62] P.S. Allison et al. "Surface Detector calibration in the Engineering Array". GAP 2002-028. July 2002.
- [63] J Abraham et al. "Trigger and aperture of the surface detector array of the Pierre Auger Observatory". In: *Nuclear Instruments and Methods in Physics Research Section A: Accelerators, Spectrometers, Detectors and Associated Equipment* 613.1 (2010), pp. 29–39.
- [64] C Bonifazi. "Angular resolution of the pierre auger observatory". In: *29th International Cosmic Ray Conference (ICRC29), Volume 7*. Vol. 7. 2005, p. 17.